PROCEEDINGS OF SPIE

SPIEDigitalLibrary.org/conference-proceedings-of-spie

Proton-induced degradation of charge transfer efficiency on FLEX CCD detectors: measurement and impact on instrument performances

François Bernard, Matej Arko, Thibaut Prod'homme, Frédéric Lemmel, Toncho Ivanov, et al.

François Bernard, Matej Arko, Thibaut Prod'homme, Frédéric Lemmel, Toncho Ivanov, Nick Nelms, Michal Miler, Matteo Taccola, Michael Francois, Peter Mario Coppo, Moreno Stagi, Emanuela De Luca, Marc Barillot, "Proton-induced degradation of charge transfer efficiency on FLEX CCD detectors: measurement and impact on instrument performances," Proc. SPIE 11852, International Conference on Space Optics — ICSO 2020, 118525F (11 June 2021); doi: 10.1117/12.2599957

SPIE.

Event: International Conference on Space Optics — ICSO 2021, 2021, Online Only

International Conference on Space Optics—ICSO 2020

Virtual Conference

30 March–2 April 2021

Edited by Bruno Cugny, Zoran Sodnik, and Nikos Karafolas

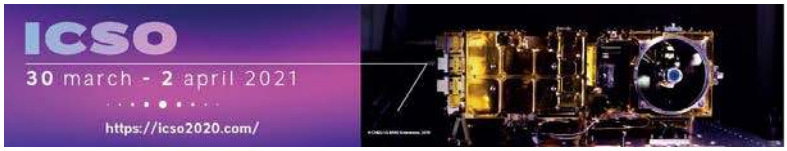

Proton-induced degradation of charge transfer efficiency on FLEX CCD detectors: measurement and impact on instrument performances

International Conference on Space Optics — ICSO 2020, edited by Bruno Cugny, Zoran Sodnik, Nikos Karafolas, Proc. of SPIE Vol. 11852, 118525F · © 2021 ESA and CNES
CCC code: 0277-786X/21/$21 · doi: 10.1117/12.2599957

Proton-induced degradation of Charge Transfer Efficiency on FLEX CCD detectors: measurement and impact on instrument performance

François Bernard[a], Matej Arko[a], Thibaut Prod'homme[a], Frédéric Lemmel[a], Toncho Ivanov[a], Nick Nelms[a], Michal Miler[a], Matteo Taccola[a], Michael François[a], Peter Coppo[b], Moreno Stagi[b], Emanuela De Luca[b], and Marc Barillot[c]

[a]European Space Agency, ESTEC, Keplerlaan 1, 2201 AZ, Noordwijk, The Netherlands
[b]Leonardo, Via A. Einstein, 35, Campi Bisenzio, 50013 Florence, Italy
[c]Thales Alenia Space France, 5, Allée des Gabians, BP 99, 06156 Cannes La Bocca Cedex, France

ABSTRACT

The exposure of Charge-Coupled Devices (CCD) to high-energy particles in space leads to a degradation of their performances. One of the observed mechanisms is the creation of defects in the CCD silicon lattice by displacement damage, inducing a reduction of the Charge Transfer Efficiency (CTE), i.e. the ability of the device to efficiently transfer the photo-induced charge to the read-out output node. Hence a reduction of the imaging quality of the detector. We present here a comparison of the modelled and measured optical quality of the FLEX CCD exposed to a high energy proton flux. The optical quality was directly measured on an irradiated flight representative device. A physical model of the detector, including an accurate modelling of the charge trapping dynamic, is used to generate synthetic scenes affected by CTE degradation from which the optical quality is assessed and compared to the measurement. Eventually the correlation of the model and the measurement will allow to accurately assess the performances of a detector exposed to space radiation environment.

Keywords: Earth observation, FLEX, Imaging sensors, CCD, simulation, modelling, Python, data analysis

1. INTRODUCTION

The Fluorescence Imaging Spectrometer (FLORIS) instrument, embarked on ESA's FLEX mission, is designed to monitor the photosynthetic activity of the terrestrial vegetation layer by measuring the chlorophyll sun-induced fluorescence signal.[1] FLORIS is a pushbroom hyperspectral imager, flying on a sun-synchronous polar orbit, which will measure the vegetation fluorescence in the spectral range between 500 nm and 780 nm at medium spatial sampling (300 m) and over a swath of 150 km. It accommodates an imaging spectrometer with a very high spectral resolution (0.3 nm), to measure the fluorescence spectrum within two oxygen absorption bands (O2A and O2B), and a second spectrometer with lower spectral resolution to derive additional atmospheric and vegetation parameters. Both spectrometers have CCDs in their focal planes.[2,3]

As reported for a number of ESA missions using CCDs either in operation or currently in development (e.g., Sentinel-4,[4] Sentinel-5, HST,[5] XMM, Gaia,[6–8] Euclid,[9–11] PLATO[12]), radiation effects may significantly impact their scientific performance if not properly studied and accounted for in the data processing. Indeed high-energy particles impacting the detectors result in the creation of CCD silicon lattice defects. Such defects act as traps, which may capture an electron from the conducting band or a hole from the valence band and keep them for a characteristic time which depends on the trap nature. As a result, not all the charge accumulated in a pixel can be transferred during the CCD image transfer. This is quantified by the degradation of the Charge transfer Efficiency (CTE). CTE is the fraction of the charge that is effectively transferred from pixel to pixel. Signal carriers caught by traps are eventually released and in this way distributed to other pixels. This affects the radiometric performance as well as the image quality. The amplitude of this charge redistribution is

For contacting the authors send correspondence to: (francois.bernard@esa.int)

determined by the parameters describing the traps created by the damaging protons (namely the trap density, the trap capture cross section and the trap release time constant which depends also on the detector operational temperature). Because the number of traps and therefore the amount of trapped charge is fixed, the relative performance degradation is higher at low signals such as, in the case of FLEX, the sun-induced fluorescence signals. For this reason a careful characterization of the CTE impact on FLORIS performance along its lifetime is of particular importance.

In this paper we present the status of an on-going study which aims at assessing the impact of in-flight degradation of CTE on the FLORIS optical performance using different and complementary approaches, namely: (i) the experimental characterization of image quality using a proton-irradiated FLEX CCD, (ii) the simulation of the CTE impact on image quality using a CCD CTE model calibrated against FLEX test data. Eventually, the simulations and on-ground characterization will be used to define a strategy for monitoring the instrument image quality over the operational life of the instrument.

2. THE FLORIS INSTRUMENT

As illustrated on Figure 1, FLORIS is composed of two separate spectrometers, sharing a common imaging telescope. The first spectrometer, referred to as Low Resolution (LR) spectrometer images the scene spectrum from 500nm to 758nm with a spectral resolution lower than 2nm. The second spectrometer, the High Resolution (HR) spectrometer, images two spectral ranges from 677nm to 697nm (centered on the O2B absorption band) and from 740nm to 780nm (centered on the O2A absorption band), both with a spectral resolution lower than 0.3nm or 0.5nm, depending on the spectral bands.[2]

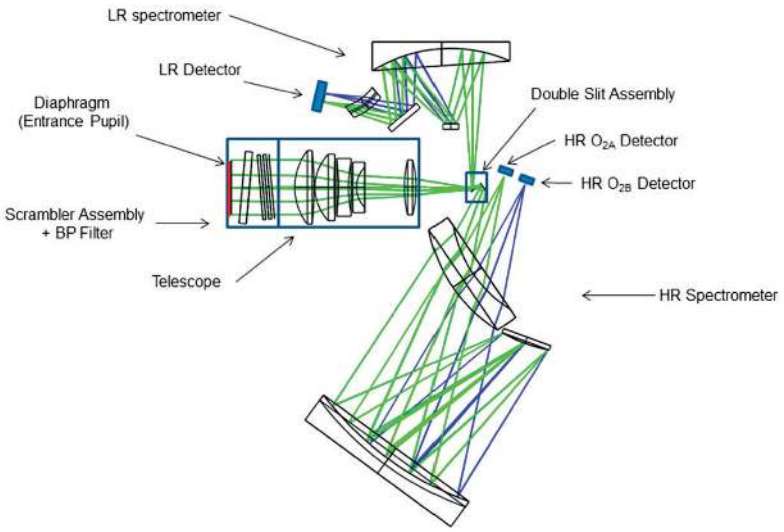

Figure 1. FLORIS optical layout

Three identical CCDs are used in FLORIS. One in the Low Resolution spectrometer focal plane and two in the High Resolution spectrometer focal plane. These detectors are based on the CCD325 from Te2V. The main characteristics of this detector are reported in Table 1, and their architecture described in Figure 2.

3. MEASUREMENT TEST DATA ON AN IRRADIATED CCD

A flight representative CCD was irradiated and measurements of optical quality were subsequently performed. The irradiation campaign as well as the optical measurements are described in the following sections.

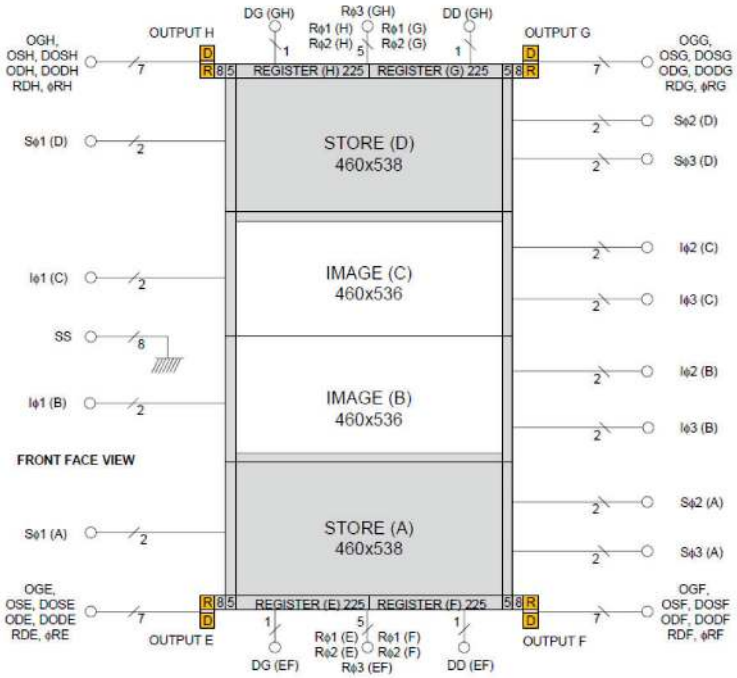

Figure 2. CCD325 chip sketch

Parameter	Specification	Comment
Type	Split frame transfer	2 zones
Image section dimensions	536 rows × 460 columns	two identical image zones
Store section dimensions	538 rows × 460 columns	two identical store sections
Pixel size (spectral × spatial)	28 μm × 42 μm	nominal acquisition: binning ×2 in spatial direction
Horizontal register	476 pixels	identical on top and bottom
Outputs	4	2 for each horizontal registers (left and right)
Vertical line transfer	800 kHz	
Register transfer rate	1.7 MHz	
Anti-blooming	none	
Pixel Full Well Capacity	2.1 Me^-	
Register Full Well Capacity	2.95 Me^-	
Read-out noise	27 e^-	
Dark current	170 e^-/s/pixel	at -35°C

Table 1. Te2V CCD325 main specifications

3.1 Irradiation campaign

A proton irradiation campaign has been performed on a dedicated model of the FLEX CCD. By adequately masking the sensor surface, four different doses were deposed on the four quadrants of the CCD. Dividing the detector into four quadrants is natural considering its architecture. As depicted on Figure 2, the image section C is transferred upwards to the store section D, while the image section B is transferred downwards to the store section A. The store section D is then read-out through the output nodes H (left) and G (right) of the serial register. Similarly the store section A is read-out in the output nodes E and F of the serial register. Each quadrant is identified by the letter of the corresponding image section, store section and output (e.g. the upper left quadrant identifier is CDH). The device was exposed to a 40-MeV proton beam, with doses per quadrant

given in Table 2

Quadrant	40-MeV proton dose [p^+/cm^2]
BAE	0.0
BAF	4.9×10^9
CDG	9.7×10^9
CDH	1.9×10^{10}

Table 2. Proton doses deposed on CCD per quadrant

The quadrant BAE is shielded from the proton beam and kept as reference area. These doses are to be compared to the worst dose expected in-orbit on the FLEX sensor (6.0×10^9 p^+/cm^2). The CDG area can therefore be considered as representative of flight conditions, with a safe margin.

3.2 Extended Pixel Edge Response measurement

Measurements of the image quality were performed at ESTEC on a dedicated test bench. Two different measurements are reported here. The first type consists in illuminating the sensor in flat field by means of an integrating sphere, and modify the CCD clocking to transfer additional pixels in order to read-out the charge delayed by CTE reduction. The CTE can be inferred from the integration of the charge measured in the over-scanned region, i.e. the deferred signal. This method is referred to as the Extended Pixel Edge Response and is illustrated on Figure 3. The signal levels of the flat illumination (1 ke^-, 3 ke^-, 7 ke^-, 10 ke^-, 20 ke^-, 50 ke^-, 100 ke^-, 500 ke^-, 1100 ke^-) were chosen to cover the operational signal range of FLORIS. The data of the EPER measurement is used as calibration measurements for the extraction of the lattice trap parameters in the model, as described in section 4.

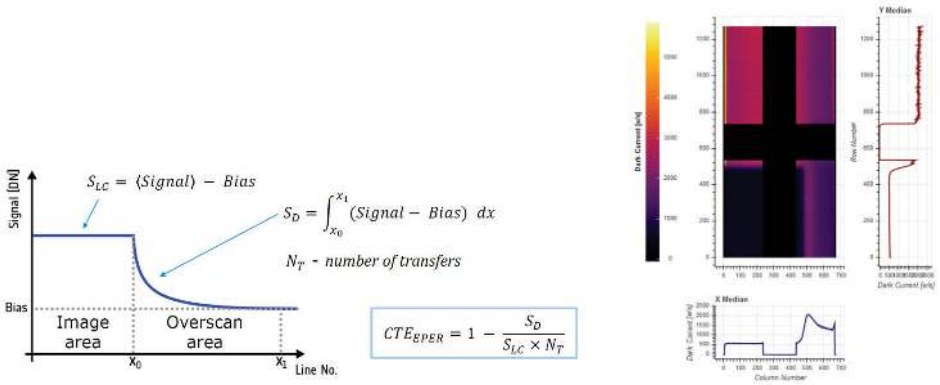

Figure 3. EPER method principle (left) and typical acquired image (right). The dark crossed-shape area in the center of the image corresponds to the over-scanned areas in the parallel direction (vertical, corresponding to image to store transfer) and serial direction (horizontal, corresponding to the transfer in the register).

3.3 USAF scene projection for measurement of Contrast Transfer Function

A direct assessment of the image quality is performed through the measurement of the Contrast Transfer Function (CTF), on the test bench shown on Figure 4. CTF is a typical figure of merit of the image quality of optical systems that is measured as the contrast of a periodic square pattern on the detector plane. Targets such as the one presented on Figure 4 contains patterns of different spatial periods, allowing to sample the CTF curve and plot it against spatial frequency.

The test is performed with a clocking sequence fully representative of the operational sequence and at the operational temperature of the detector (238 K). Four different patterns are chosen in order to sample the CTF

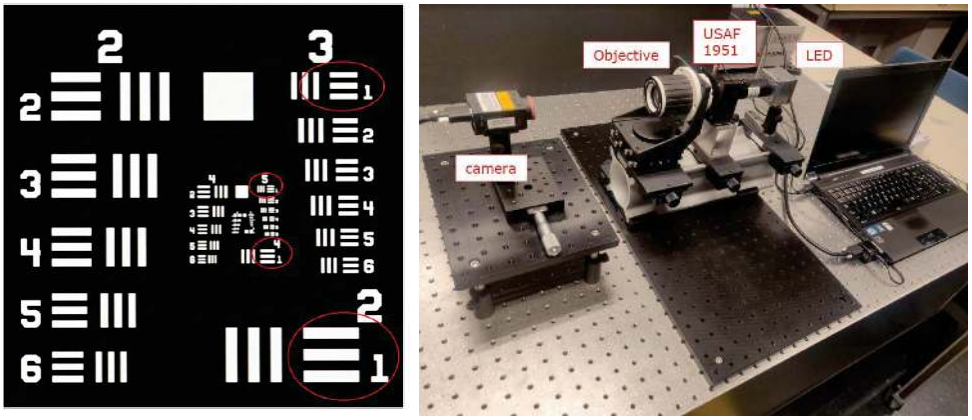

Figure 4. Left: USAF CTF target; Right: test bench composed of a light source (LED) illuminating the USAF target, which is then imaged on the detector thanks to a relay objective. On this picture, a service camera is located in the focal plane for verifying the alignment of the setup. The FLEX CCD is located at the same location as the service camera for the CTF measurement.

curve up to the Nyquist frequency (i.e. 11.9 lp/mm for 42 μm pixels). The patterns are projected at the two edges of each detector image quadrant (close to the center of the detector, and close to the store area) in order to cover the highest and lowest, respectively, number of transfers through the image section. These positions correspond to worst and best cases, respectively, regarding the impact of the CTE on the image quality. Additionally the pattern are slightly tilted in order to reach a sub-pixel sampling of the pattern profiles. Finally the CTF is measured at three signal levels (1 ke$^-$, 3 ke$^-$ and 10 ke$^-$) and two detector temperatures (238 K, 248 K).

The effect of CTE on the instrument optical performances can be assessed thanks to the Modulation Transfer Function (MTF). For spatial frequencies lower than the Nyquist frequency, the CTF is directly proportional to the MTF, which allows to relate the CTF measurements to the performance model. A relation between MTF and Charge Transfer Efficiency can be found in the literature:[13]

$$MTF_{CTE}(f) = \exp\left[-N_t(1-\mathrm{CTE})\left(1-\cos\left(\pi\frac{f}{f_{nyq}}\right)\right)\right] \quad (1)$$

where N_t is the number of transfer, f is the spatial frequency and f_{nyq} is the Nyquist frequency. This formula is inverted to extract the CTE from the CTF measurement. The detector MTF is then derived as $MTF_{det}(f) = MTF_{pixel}(f) \times MTF_{CTE}$ with $MTF_{pixel}(f) = \mathrm{sinc}(\pi fp)\mathrm{sinc}(\pi fx)$ representing the MTF response for a pixel size p (42 μm) and cross-talk x (18 μm), fitting the detector MTF measured on-ground. The results of the measurements are presented on Figure 5 and compared to the CTF model used for instrument performance analyses.

One of the key performance to monitor in order to assess the severity of the CTE effect is the spatial resolution, through the full width at half maximum (FWHM) of the point spread function. Figure 6 shows the point spread function at the end of the operational life, including the effect of CTE measured in the CDG quadrant as described above. This figure illustrates that the FWHM of the PSF remains within the range required for FLEX (100 μm in the focal plane, equivalent to roughly 360 meters on ground, *i.e.* 1.2 times the spatial sampling distance (SSD)).

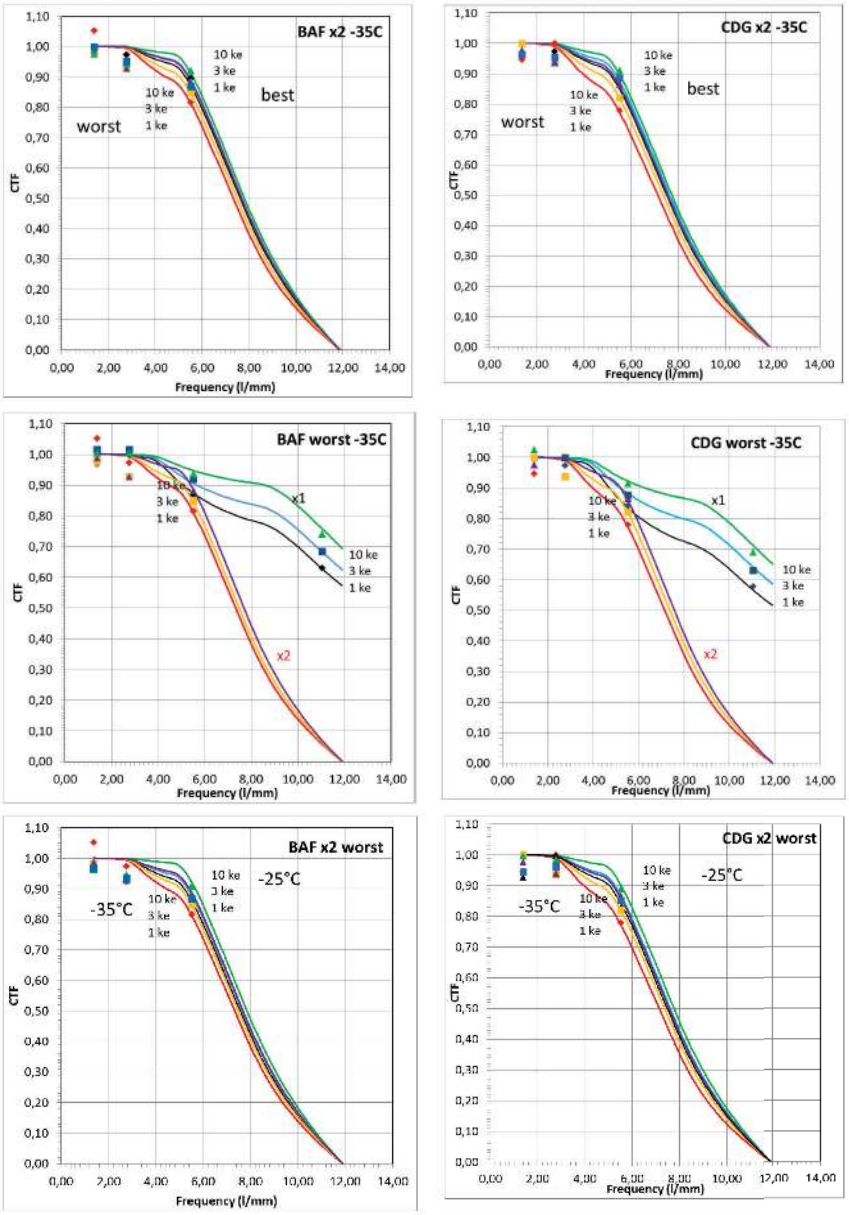

Figure 5. CTF measurement results for two irradiated quadrants (left: 4.9 $\times 10^9$ p^+/cm^2, right: 9.7 $\times 10^9$ p^+/cm^2) The two plots on the top compare the CTF measured at the best and worst case positions of the image quadrant at 238 K and for binned pixels. The two center plots presents the results for the unbinned case and the operational binned case, at worst case position, and 238 K. The two bottom plots compares the results at 238 K and 248 K, at worst case position and for binned pixels. The solid lines is computed from the MTF model, converted to CTF to be compared to the measurement points.

4. CTE MODELLING AND SIMULATIONS OF FLEX-LIKE IMAGES

Using the Pyxel framework[14] - a python-based detection simulation tool - we first calibrate CDM (Charge Distortion Model)[15] - a commonly-used CTE model - against laboratory test data acquired under FLEX representative

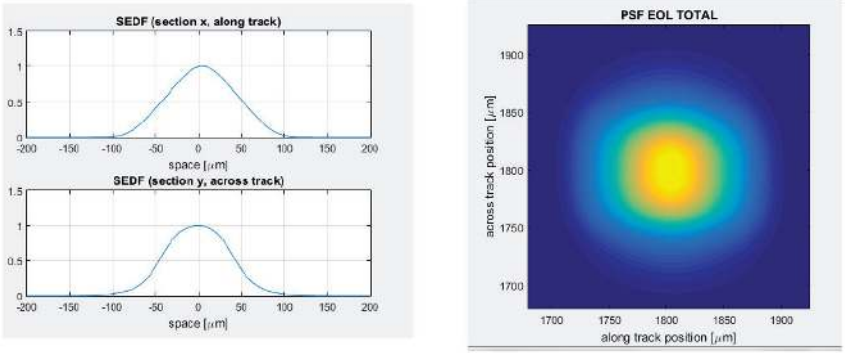

Figure 6. Optical point spread function of the instrument (2-D false color map is presented on the right and the horizontal and vertical cross-sections are presented on the left), including the CTE effect measured on the irradiated CCD. The considered proton dose is 9.7 $\times 10^9$ p^+/cm^2, representative of the total dose received by the CCD at the end of its operational life in orbit. The PSF is represented in the focal plane, hence the distances along both axes are given in micrometers.

conditions. Once calibrated we use this model to degrade images and measure the impact of CTE on image quality. Ultimately this model can be used to generate synthetic FLEX-representative spectra including the effect of degraded CTE, which can be useful in assessing the impact of CTE in the final scientific measurements and devising an in orbit monitoring and mitigation strategy. In the following we present first the calibration of CDM - methodology and results-, and then the simulation of degraded images to measure the impact of CTE on the detector CTF. The Pyxel jupyter notebooks used for the CTE calibration and the simulation of CTE effects on the FLEX CTF are openly available online in the public repository Pyxel Data.[16]

4.1 Calibration of the CTE model

CDM is a fast analytical model of CTE in CCDs, it computes at once the effects on a given image of the charge trapping and de-trapping of traps during parallel and/or serial transfer. CDM can simulate the effect of an arbitrary number of trap species parametrised through their trap density, capture cross section, and release time constant. CDM makes use of an extra parameter β in order to link charge packet volume and charge density for a given signal level. CDM has not been designed for accuracy and realism but for flexibility and speed; it was developed in the context of Gaia data processing with the aim of calibrating out CTE effects. It is capable of reproducing fairly well test data (from EPER trails to spectra, point sources and extended objects) and give a good idea of the type of trap species in presence and can be used to investigate the possible CTE effects on images once calibrated over a representative and large set of test data.

We do so by using the so-called calibration running mode of Pyxel. This mode makes use of evolutionary algorithms implemented in the library PyGMO,[17] a Python library for massively parallel optimization. The two main inputs of the calibration mode in Pyxel are: initial data to which the models are applied during the pipeline and target data which serves as a benchmark for computing the goodness of fits with given parameter sets, in PyGMO nomenclature: computing the fitness of individuals. Here, the target data is derived from the laboratory test measurement presented in Section 3: to speed up the simulation process, we do not simulate an entire image but instead simulate the transfers over a unique CCD column for this we thus average the flat field and overscan in the serial direction over a given irradiated region to obtain a representative average parallel charge profile. We used the data acquired at T = 238 K, for 6 different signal levels: $1ke^-$, $3ke^-$, $7ke^-$, $10ke^-$, $20ke^-$ and $100ke^-$, and over the irradiated region CDH, the quadrant with the highest proton dose, this is 1.9×10^{10} p^+/cm^2 (see Table 2). The degraded CTE can be seen in the form of charge trails, as shown in figure 7. The simulation input charge profile is generated from the same test data, for which only the flat field part of the image is kept.

The free parameters during calibration are: the electron cloud expansion coefficient β, the trap release times τ_r and the trap densities n_{tr}, all for the parallel direction. We choose the number of 4 different trap species; this translates into a total of 9 free parameters. The exact same calibration procedure was repeated with 3 and 5

β			0.312
Trap no.	$\tau_r[ms]$	N_{tr}	Trap species
1	0.29	73.98	/
2	4.16	9.40	Divacancy (-/0)
3	8.81	16.06	Divacancy (-/0)
4	40.40	2.85	E-center (Phosphorous Vacancy complex)

Table 3. Optimal set of parameters resulting from the described calibration procedure and the possible corresponding trap species (see[4] for a more complete overview and discussion of trap species).

trap species; for 3 traps species the achieved fitness is poorer, while using 5 traps species does not improve the solution achieved with 4. Because of the large number of free parameters, we run the simulation on a cluster of computers, which enables us to probe large number of potential parameter sets (aka individuals), while still keeping the total time of simulation rather short ($<$ 24 hours). We use a total number of 40 workers with 80 threads to evolve 20000 individuals for 2500 generations.

The presented calibration method ultimately leads to the set of CDM parameters presented in Table 3. The associated quality of fit can be seen in Fig. 7 and Fig. 8. And the representativity of this calibrated set of parameter against other best fit sets is shown in Fig. 9 giving us confidence that the found set of parameter is close to a global minimum. For this temperature, the release time constant found, corresponds rather well to the E centre (Phosphorous Vacancy complex) for the longest release time constant and the divacancy complex for the intermediate constants. The shortest show a very high trap density which seems unrealistic, it also does not immediately seem to correspond to a trap species found in the literature. This result for the shortest release time constant could either point at one of CDM's shortcoming - namely the fact that CDM does not simulate properly trapping at time scale shorter than a transfer period - or the fact that the test data contains a sharp edge response which is not due to CTE but some electronics effect (this could be verified looking at the trails in the non-irradiated region of the CCD). The use of this very short release time constant in simulating CTE effects on FLEX images has thus to be done with caution.

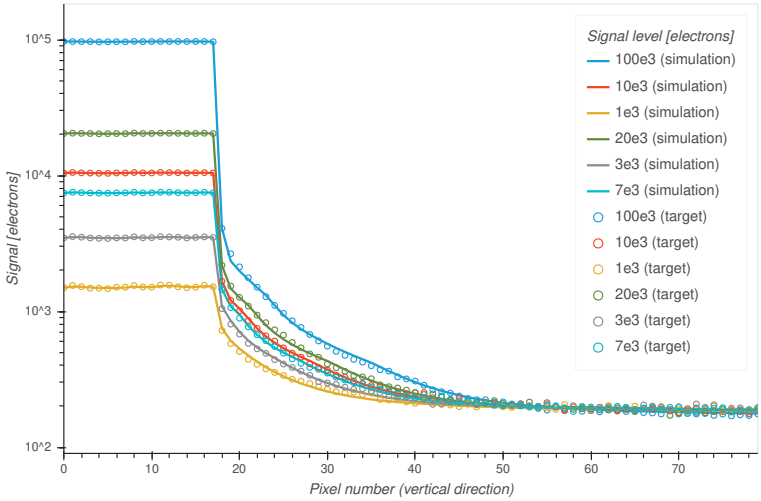

Figure 7. The target test data (circles) and the simulated charge profiles (lines) after calibration, giving a visual impression of how well CDM can fit the FLEX test data over a wide range of signal level.

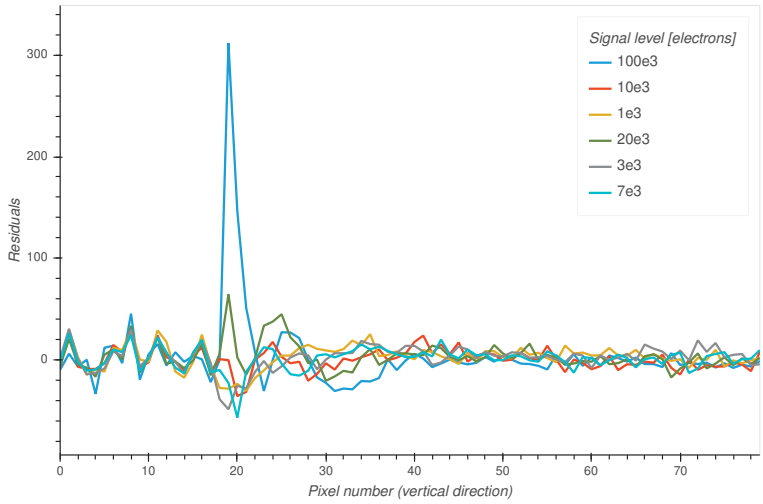

Figure 8. The fit residuals for the data shown above. It shows that the fit is not biased towards higher signal level as a result of the figure of merit compensation scheme put in place during calibration; namely the figure of merit is weighted by the signal level. The total fitness of an individual is computed from residuals.

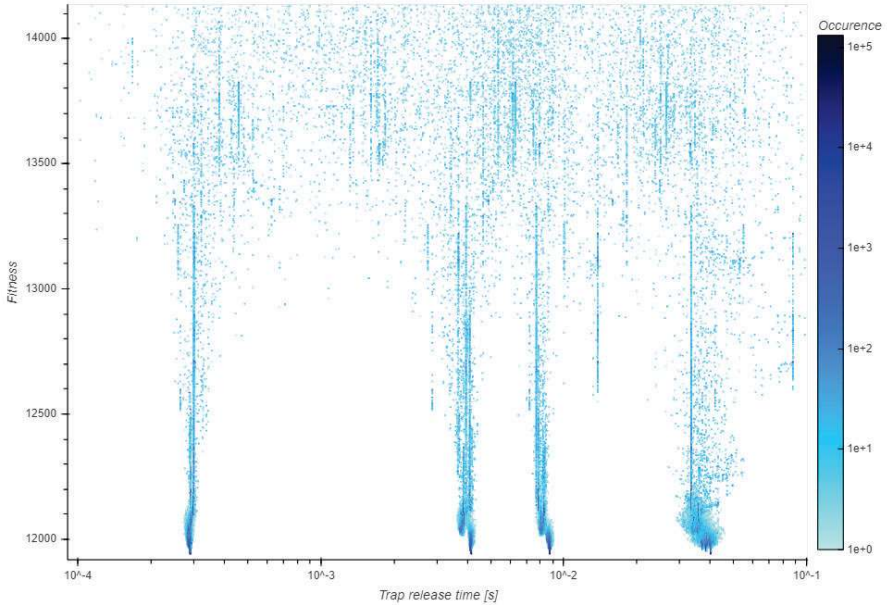

Figure 9. Two-dimensional histogram of trap release times vs. fitness. By plotting the histogram in this way we can see how the optimal set of trap release time parameters is found over time in the process of calibration. Points for computing the histogram are the four trap release times τ_r of the 20 best parameter sets (individuals) from each evolution and from each of the processor cores (islands). Parameter space is homogeneously and randomly populated at the start and gets more constrained to the area around the best solutions at the end, with best solutions showing the highest occurrence. This figure illustrate the advantage of this optimised genetic algorithm; it probes a large chunk of the parameter space and converge to what can be considered to a global minimum since the evolution of different islands ends up with very similar trap species and β parameter.

4.2 Generation of synthetic CTF measurements and comparison with test data measurement

We use the calibrated CDM model to generate synthetic CTF curves for comparison with the laboratory measurements done on USAF targets (unbinned case), described in section 3.3. We achieve this by applying the model to images of periodic square patterns and observing the change of contrast as a function of both spatial frequency and signal level. As in laboratory measurements, we do so for two different regions: BAF and CDG, and for three different signal levels: $1ke^-$, $3ke^-$ and $10ke^-$. For this purpose the parametric mode of Pyxel can be utilized, which allows us to run pipelines and apply models for many different sets of input model parameters. We create and include in Pyxel a simple illumination model of periodic square patterns, with signal level and spatial frequency as parameters. The patterns are tilted at a small angle as in section 3.3, again to ensure sub-pixel sampling of the pattern profiles.

The calibration of CDM model is done on the quadrant with the highest proton dose (CDH) and laboratory measurements are done on the quadrants with lower proton dose (CDG and BAF), thus we adjust the trap densities accordingly to match the predicted trap density in the CDG and BAF regions. Because of unreliability of the fastest trap result, explained in section 4.1, the effect of the fastest trap is omitted from the model. As is expected and seen in the laboratory measurement data, the non-irradiated detector does not show ideal contrast transfer over all spatial frequencies. We approximate the contrast degradation of a non-irradiated detector by convolving the patterns with a simple Gaussian point spread function with $\sigma = 0.28\ px$. This way we match the values of simulated and measured CTF curves at the highest spatial frequency and for the case of non-irradiated detector at the value of 0.85. The combined effect of CDM and convolution with a narrow Gaussian on tilted periodic patterns can be seen in figure 10. From the patterns we compute points for the CTF curves as $(I_{max} - I_{min})/(I_{max} + I_{min})$, where I is the intensity in the region of interest.

The result of the simulated CTF curves versus the laboratory measurements is shown in figure 11, together with the data for the non-irradiated case. There is a clear discrepancy between CTF simulations and measurements; the laboratory measurements showing much better contrast response. Comparing the two it can be seen that in the case of simulated CTF curves there is first a quick decay of contrast even at small spatial frequencies and second a large dispersion of curves for different signal levels. Whether the mismatch is a result of a difference in CTF derivation procedure or simply a result of a parameter set that has not reached the global minimum is yet to be researched. It is already known that the CTF measurements have been taken at a temperature 6 K lower than the target data used to calibrate CDM, and that the clocking scheme used during the test campaigns may differ too greatly from the simplifications used in the simulations. Based on the findings, the model and CTF calculation will have to be refined in order to validate and match the simulations with the measurements. This way it could be used in the future for generation of synthetic FLEX-representative spectra with the effects of CTE degradation.

5. CONCLUSION

In the previous sections we have presented the results of measurements and modeling of the effect on the FLEX CCD of Charge Transfer Inefficiency induced by proton damage in the crystalline lattice of the detector. A flight representative device has been irradiated for this purpose and optical measurements were then performed. The measurement results presented above have been used for two purposes: first to have a direct evaluation of the degradation of FLORIS optical performance through the measurement of the Contrast Transfer Function of the CCD. Second, to generate calibration input data to feed into the detector model (CDM). This calibration data is used to derive the trap species parameters, by fitting it thanks to an evolutionary algorithm. After the calibration step, the model is then used on synthetic scenes similar to the measurement scenes, and compute the CTF from these synthetic scenes. The outputs of the model are compared to the test results and show discrepancies which are so far unexplained. The next phase of this work will be dedicated to understand and solve this mismatch, aiming at eventually obtain an accurate modelling framework for assessing the optical quality of a detector affected by Charge Transfer Inefficiency.

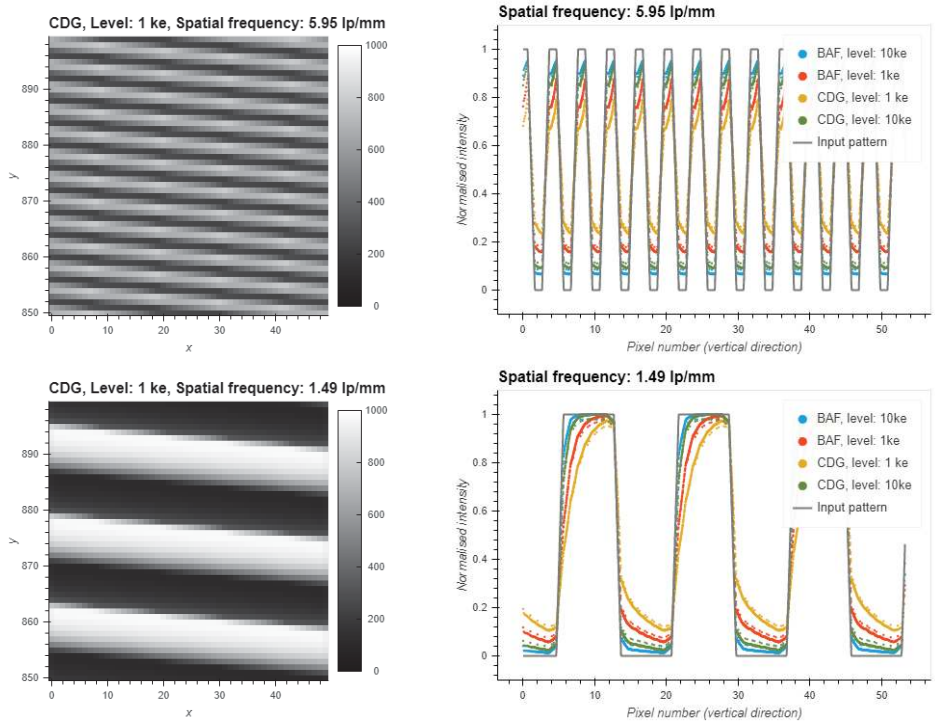

Figure 10. Effect of calibrated CDM model on the periodic patterns. On the left we can see the slanted periodic patterns for different spatial frequencies: 5.95 and 1.49 lp/mm, where trap densities correspond to region CDG and initial signal level of the patterns is 1 ke^-. On the right there are normalized cross sections of the patterns at the same spatial frequencies as in the left images, sampled at a sub-pixel resolution. The patterns are shown for different quadrants (CDG and BAF) and for different signal levels of the input pattern, this way the drop in contrast can be observed. Final contrast is computed using this cross-sections using the maximal and minimal values of the curves.

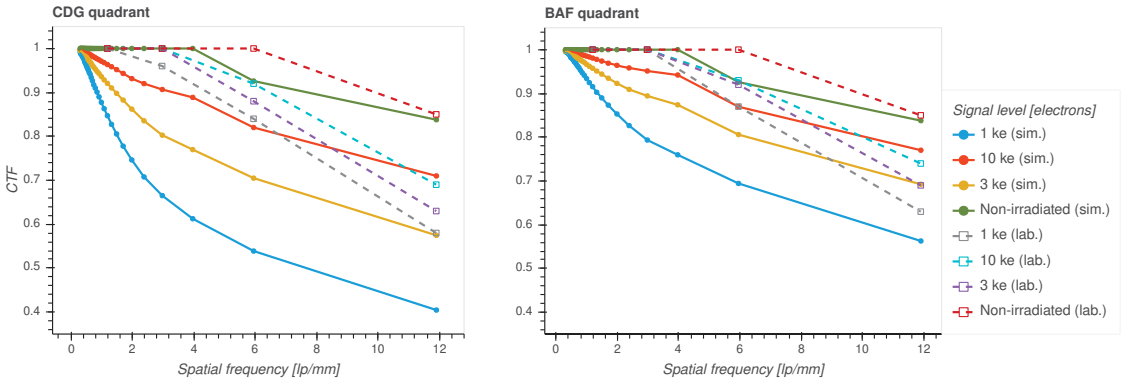

Figure 11. Comparison of CTF measurements (dashed line) and CTF results from the simulation (solid line) for two different quadrants (CDG and BAF) and different signal levels, including data of the non-irradiated detector. There is a noticable difference between simulations and measurements, especially at low spatial frequencies and in the dispersion of simulation data for different signal levels.

REFERENCES

[1] Drusch, M., Moreno, J., Del Bello, U., Franco, R., Goulas, Y., Huth, A., Kraft, S., Middleton, E. M., Miglietta, F., Mohammed, G., Nedbal, L., Rascher, U., Schüttemeyer, D., and Verhoef, W., "The fluo-

rescence explorer mission concept—esa's earth explorer 8," *IEEE Transactions on Geoscience and Remote Sensing* **55**(3), 1273–1284 (2017).

[2] Coppo, P., Taiti, A., Pettinato, L., Francois, M., Taccola, M., and Drusch, M., "Fluorescence imaging spectrometer (floris) for esa flex mission," *Remote Sensing* **9**(7) (2017).

[3] Coppo, P., Pettinato, L., Nuzzi, D., Fossati, E., Taiti, A., Gabrieli, R., Campa, A., Taccola, M., Bézy, J.-L., Francois, M., Erdmann, L. H., Triebel, P., and Lehr, D., "Instrument predevelopment activities for FLEX mission," *Optical Engineering* **58**(7), 1 – 25 (2019).

[4] Prod'homme, T., Belloir, J. M., Weber, H., Bazalgette Courrèges-Lacoste, G., Meynart, R., Nowicki-Bringuier, Y. R., Caron, J., Levillain, Y., Woffinden, C., Lord, B., and Mackie, R., "Radiation-induced charge transfer inefficiency in charge-coupled devices: Sentinel-4 CCD pre-development as a case study," in [*Sensors, Systems, and Next-Generation Satellites XVIII*], Meynart, R., Neeck, S. P., and Shimoda, H., eds., *Society of Photo-Optical Instrumentation Engineers (SPIE) Conference Series* **9241**, 92410Y (Oct. 2014).

[5] Massey, R., Schrabback, T., Cordes, O., Marggraf, O., Israel, H., Miller, L., Hall, D., Cropper, M., Prod'homme, T., and Niemi, S.-M., "An improved model of charge transfer inefficiency and correction algorithm for the Hubble Space Telescope," **439**, 887–907 (Mar. 2014).

[6] Prod'homme, T., Holl, B., Lindegren, L., and Brown, A. G. A., "The impact of CCD radiation damage on Gaia astrometry - I. Image location estimation in the presence of radiation damage," **419**, 2995–3017 (Feb. 2012).

[7] Holl, B., Prod'homme, T., Lindegren, L., and Brown, A. G. A., "The impact of CCD radiation damage on Gaia astrometry - II. Effect of image location errors on the astrometric solution," **422**, 2786–2807 (June 2012).

[8] Crowley, C., Kohley, R., Hambly, N. C., Davidson, M., Abreu, A., van Leeuwen, F., Fabricius, C., Seabroke, G., de Bruijne, J. H. J., Short, A., Lindegren, L., Brown, A. G. A., Sarri, G., Gare, P., Prusti, T., Prod'homme, T., Mora, A., Martín-Fleitas, J., Raison, F., Lammers, U., O'Mullane, W., and Jansen, F., "Gaia Data Release 1. On-orbit performance of the Gaia CCDs at L2," **595**, A6 (Nov. 2016).

[9] Israel, H., Massey, R., Prod'homme, T., Cropper, M., Cordes, O., Gow, J., Kohley, R., Marggraf, O., Niemi, S., Rhodes, J., Short, A., and Verhoeve, P., "How well can charge transfer inefficiency be corrected? A parameter sensitivity study for iterative correction," **453**, 561–580 (Oct. 2015).

[10] Prod'homme, T., Verhoeve, P., Oosterbroek, T., Boudin, N., Short, A., and Kohley, R., "Laboratory simulation of Euclid-like sky images to study the impact of CCD radiation damage on weak gravitational lensing," in [*High Energy, Optical, and Infrared Detectors for Astronomy VI*], Holland, A. D. and Beletic, J., eds., *Society of Photo-Optical Instrumentation Engineers (SPIE) Conference Series* **9154**, 915414 (July 2014).

[11] Prod'homme, T., Liebing, P., Verhoeve, P., Menyaylov, I., Lemmel, F., Smit, H., Blommaert, S., Breeveld, D., and Shortt, B., "A smartphone-based arbitrary scene projector for detector testing and instrument performance evaluation," in [*Society of Photo-Optical Instrumentation Engineers (SPIE) Conference Series*], *Society of Photo-Optical Instrumentation Engineers (SPIE) Conference Series* **11454**, 1145426 (Dec. 2020).

[12] Prod'homme, T., Verhoeve, P., Lemmel, F., Smit, H., Blommaert, S., van der Luijt, C., Visser, I., Beaufort, T., Levillain, Y., and Shortt, B., "Comparative Study of Cryogenic Versus Room-Temperature Proton Irradiation of N-Channel CCDs and Subsequent Annealing," *IEEE Transactions on Nuclear Science* **66**, 134–139 (Jan. 2019).

[13] Janesick, J. R., [*Scientific Charge-Coupled Devices*], SPIE Press, Bellingham, Washington (2001). ISBN 0-8194-3698-4.

[14] Prod'homme, T., Lemmel, F., Arko, M., Serra, B., George, E., Biancalani, E., Smit, H., and Lucsanyi, D., "Pyxel: the collaborative detection simulation framework," in [*Society of Photo-Optical Instrumentation Engineers (SPIE) Conference Series*], *Society of Photo-Optical Instrumentation Engineers (SPIE) Conference Series* **11454**, 1145408 (Dec. 2020).

[15] Short, A., Crowley, C., de Bruijne, J. H. J., and Prod'homme, T., "An analytical model of radiation-induced Charge Transfer Inefficiency for CCD detectors," *Monthly Notices of the Royal Astronomical Society* **430**(4), 3078–3085 (2013).

[16] "Pyxel Data gitlab repository." https://gitlab.com/esa/pyxel-data.
[17] Biscani, F. and Izzo, D., "A parallel global multiobjective framework for optimization: pagmo," *Journal of Open Source Software* **5**(53), 2338 (2020).